The Astrophysical Journal, 625:556–562, 2005 May 20

RESPONSE FUNCTIONS OF THE ULTRAVIOLET FILTERS OF *TRACE* AND THE DETECTABILITY OF HIGH-FREQUENCY ACOUSTIC WAVES

Astrid Fossum and Mats Carlsson
Institute of Theoretical Astrophysics, P.O. Box 1029 Blindern, N-0315 Oslo, Norway
Received 2005 January 3; accepted 2005 February 10

ABSTRACT

We have used detailed non-LTE radiation hydrodynamic simulations to investigate the detectability of high-frequency acoustic waves with the *Transition Region And Coronal Explorer* (*TRACE*). A broad spectrum of acoustic waves are fed into the computational domain at the lower boundary of the model atmosphere, and *TRACE* UV continuum intensities are calculated by folding the derived intensities with the *TRACE* filter transmission functions for the 1700 and 1600 filters. Power spectra, phase diagrams, and intensity response functions are calculated, and intensity formation heights are derived. The simulations show that the average response height of the 1700 and 1600 passbands are 360 and 430 km, with widths of 325 and 185 km. The width of the *TRACE* intensity response functions reduces the power of the intensity oscillations considerably, but if waves are present with power enough to be of importance for the energy balance of the chromosphere, they should be detectable at least up to 40 mHz in the absence of instrumental noise, especially in the 1600 passband. The phase difference between the synthesized 1600 and 1700 *TRACE* intensities follows the curve expected for propagating acoustic waves up to 15 mHz. For higher frequencies the phase difference decreases and approaches zero before the coherence drops down, similar to the observed behavior. This is explained by the double-peaked nature of the response function for the 1700 intensities.

Subject headings: instrumentation: miscellaneous — Sun: chromosphere — Sun: UV radiation — waves

1. INTRODUCTION

Acoustic waves were suggested by Biermann (1948) and Schwarzschild (1948) to play an important part in the heating of the solar chromosphere and corona. Athay & White (1978, 1979a, 1979b) and White & Athay (1979a, 1979b) analyzed observations of ultraviolet spectral lines taken with *OSO 8*. They found observational evidence of acoustic waves of periods from 300 to 30 s in the chromosphere, but with a total energy flux 2 orders of magnitude lower than needed to balance the radiative losses from the chromosphere. The upper limits to the acoustic flux derived from line widths showed that the lower chromosphere may be heated by acoustic waves of high frequency but that a different mechanism heats the upper chromosphere, transition region, and corona.

Heating of the lower and middle chromosphere by high-frequency acoustic waves got additional support from theoretical studies of the generation of acoustic waves in the solar convection zone. These studies showed a peak in the acoustic spectrum around 50 s period (Musielak et al. 1994; Fawzy et al. 2002). However, results from high-resolution numerical simulations of convection do not support these results but instead indicate a decreasing power as function of frequency (Goldreich et al. 1994; Stein & Nordlund 2001).

Observationally it is difficult to detect high-frequency acoustic waves for two reasons. First, the seeing causes image motion that introduces a false high-frequency component in ground-based observations and makes these waves hard to observe. Second, for both ground-based and space-based observations, the signal we get from high-frequency waves is weakened by the width of the response function. Wunnenberg et al. (2002) have summarized the various attempts at detecting high-frequency waves, and we refer the reader to them for further background.

The *Transition Region And Coronal Explorer* (*TRACE*) instrument (Handy et al. 1999) should in principle be a nice instrument for detecting high-frequency acoustic waves. Because of its orbit outside of the Earth's atmosphere we do not have any seeing disturbances. Using high-cadence observations with the ultraviolet passbands (1700, 1600, and 1550 Å) that sample the upper solar photosphere and low chromosphere, we get the opportunity not only to look at power diagrams, but also to study the phase properties of the waves.

Krijger et al. (2001) tried to detect high-frequency acoustic waves using image sequences from *TRACE* in these three UV passbands. They used two different time series of 354 and 612 images with an average cadence of 15 and 21 s, respectively. The image subfields were divided into network/internetwork depending on the average brightness of the pixels. The data were then Fourier analyzed, giving power, coherence, and phase difference information. The results showed that, except for a peak at about 3.33 mHz, the power steadily decreased toward 20 mHz, where it flattened out. Plotting the phase differences showed that for the lowest frequencies the 1600 Å intensity lead the 1700 Å intensity, which according to the authors is due to internal gravity waves. The phase difference then gradually increased up to about 7 mHz, with the 1600 Å lagging the 1700 Å. Above 7 mHz the difference decreased. In earlier studies (e.g., Deubner et al. 1984; Deubner & Fleck 1990) atmospheric seeing has been set as the reason for this decline. However, *TRACE* observations are not troubled by seeing. Similar effects may come from spacecraft jitter, but careful alignment procedures were designed to minimize these effects. Krijger et al. attributed the phase difference decline in their data as well as the older ground-based data to acoustic waves that are steepening into weak shocks on their way up.

Using a direct reliability test of the phase differences, Krijger et al. (2001) concluded that the reliability of the spectra is limited to below 15 mHz. This is due to the nonsimultaneity of the imaging in the different passbands. The sequential nature of *TRACE*'s filter wheel switching between passbands combined

with the sampling irregularity is the major contributor of phase difference noise.

Krijger et al. (2001) did not find any high-frequency waves above 15 mHz, but is that only due to noise, or is it also because the small spatial wavelength of the high-frequency acoustic waves fits within the response function width so only a fraction of the power is detectable? In this paper we aim to answer this question.

Carlsson & Stein (2002) found that high-frequency waves are heavily damped in the upper photosphere by radiation. Numerical simulations show that at 10 s period only 1% of the generated acoustic energy flux remains at a height of 500 km. They state that it would be possible for waves within the range of 20–50 mHz to play an important role for the energy balance of the upper chromosphere. These waves have long enough periods not to be completely damped in the upper photosphere, while they have short enough periods to be largely undetected observationally. We look at the possibility of detecting high-frequency acoustic waves between 20 and 50 mHz using *TRACE* filters in the 1600 and 1700 Å continuum. A regularity of the sampling is assumed. To achieve this we use numerical simulations of the propagation of acoustic waves to make artificial observations, and these are then analyzed in the same way as real observations.

The outline of the paper is as follows. First we describe the numerical method and model used in our simulations. In § 3 we discuss the power plots, response functions, and phase difference plots. To simulate the effects of the *TRACE* instrument, we add Poisson noise to the calculated intensities and see how that affects the results. We also make some simple studies of sine waves to look at the properties of the response functions and the Fourier analysis method itself. In § 4 we give our conclusions.

2. NUMERICAL SIMULATIONS

The numerical simulations we used to study the detectability of high-frequency waves were done with the radiation hydrodynamics code by Carlsson & Stein (1990, 1992, 1994, 1995, 1997, 2002). The code aims to include the most essential physical processes in a one-dimensional model without magnetic fields, including a self-consistent treatment of the radiation field and matter, a detailed treatment of the non-LTE thermodynamics, and accurate fluid treatments of shocks.

The one-dimensional equations of mass, momentum, energy, and charge conservation are solved together with the non-LTE radiative transfer and population rate equations, implicitly on an adaptive mesh. Advection is treated using van Leer (1974)'s second-order upwind scheme to ensure stability and monotonicity in the presence of shocks. An adaptive mesh is used (Dorfi & Drury 1987) in order to resolve the regions where the atomic level populations are changing rapidly (such as in shocks). The equations are solved simultaneously and implicitly to ensure self-consistency and stability in the presence of radiative energy transfer, stiff population rate equations, and to have the time steps controlled by the rate of change of the variables and not by the small Courant time for the smallest zones. A linearization method is used to solve the radiative transfer (Scharmer & Carlsson 1985), but with a pentadiagonal approximate lambda operator (Rybicki & Hummer 1991) instead of the global Scharmer operator. The effects of nonequilibrium ionization, excitation, and radiative energy exchange from several atomic species (H, He, and Ca) on fluid motions and the effect of motion on the emitted radiation from these species are calculated. We model hydrogen and singly ionized calcium by

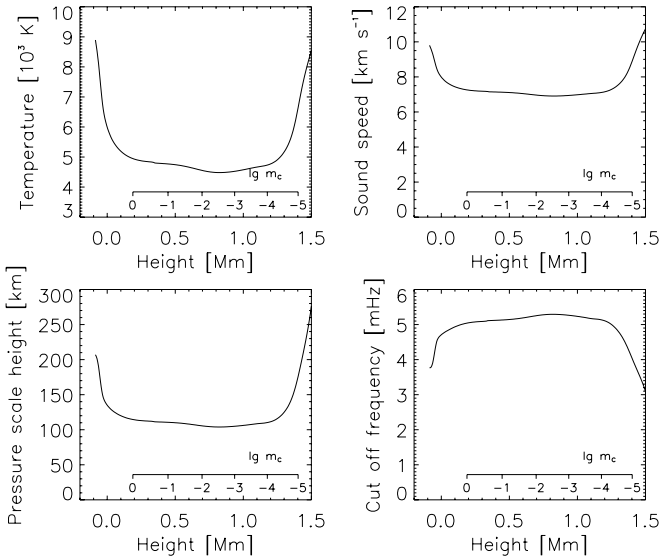

FIG. 1.—Temperature, sound speed, pressure scale height, and acoustic cutoff frequency as functions of height in the starting atmosphere; lg(column mass) is given as a secondary scale.

six-level atoms and helium with a nine-level atom. For helium we collapse terms to collective levels and include the $1s^2$, $2s$, and $2p$ terms in the singlet system and the $2s$ and $2p$ terms in the triplet system of neutral helium, and the $1s$, $2s$, and $2p$ terms of singly ionized helium. In addition we include doubly ionized helium. We include in detail all transitions between these levels. For singly ionized calcium they are the H and K resonance lines, the infrared triplet, and the photoionization continua from the five lowest levels. Continua from elements other than H, He, and Ca are treated as background continua in LTE, using the Uppsala atmospheres program (Gustafsson 1973); 1000 depth points were used in order to properly resolve short-wavelength, high-frequency acoustic waves also.

The opacity within the *TRACE* 1600 and 1700 bands is dominated by bound-free opacity from neutral silicon and by a very large number of lines from various elements. To get the silicon opacity right, it is important to solve the rate equations for silicon. Since the solution for silicon has very little effect on the thermodynamics, this can be done after the fully coupled equations described above have been solved. We thus treat silicon as a minority ion and solve the non-LTE rate equations for silicon with the density and electron density as functions of height and time as given from the fully coupled solution. We employ an eight-level plus continuum model atom for silicon with photoionization data from the opacity project (Cunto et al. 1993). We assume full statistical equilibrium of silicon at each time step, thus neglecting possible effects of slow ionization/recombination. Trial simulations including the full time-dependent solution for silicon indicate that statistical equilibrium is a good approximation. Line blanketing is included by sampling the opacity at 0.01 nm intervals in the *TRACE* passbands using the opacity data of Kurucz & Bell (1995). We include scattering in the calculation of the source functions of the spectral lines with a scattering fraction from a two-level approximation with the collisional deexcitation calculated from Van Regemorter's (1962) formulae.

The initial atmosphere is in radiative equilibrium. The basic quantities for the initial atmosphere are shown in Figure 1. The sound speed is approximately 7 km s^{-1}, and the cutoff frequency is about 5 mHz. The upper boundary is a corona at 10^6 K at 10^4 km with a transmitting boundary condition. Incident

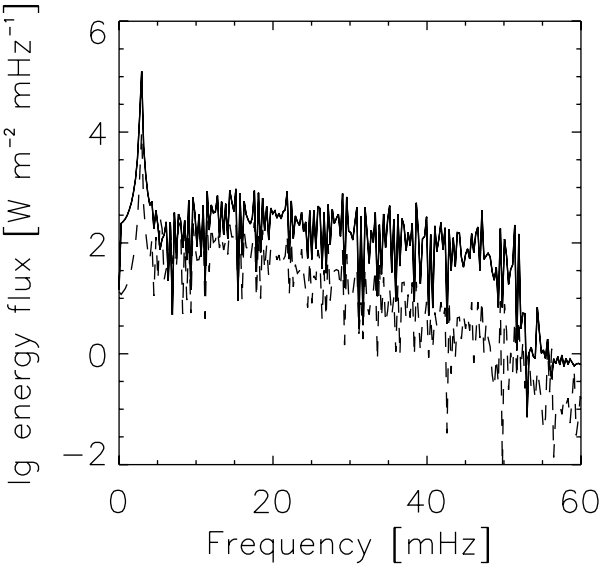

FIG. 2.—Acoustic energy flux of the piston at the bottom of the computational domain (*solid line*) and at a height of 400 km (*dotted line*) as a function of frequency.

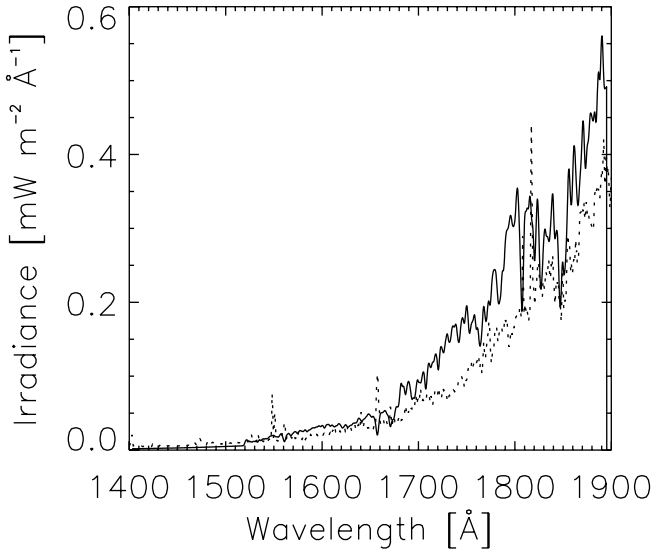

FIG. 3.—Simulated irradiance convolved with a Gaussian kernel (*solid line*), compared to observed irradiance from the *ATLAS-3* SUSIM mission on 1994 November 13 (*dotted line*). The resolution is 0.15 nm.

radiation from the corona taken from observations (Tobiska 1991) is included. This causes ionization in the helium continua in the upper chromosphere. Waves are driven through the atmosphere by a piston located at the bottom of the computational domain (86 km below $\tau_{500} = 1$). The piston velocity is taken from P. Ulmschneider's (1998, private communication) theoretical model for wave excitation, and this is the first time that high-frequency pistons are used in these simulations.

Figure 2 shows the acoustic energy flux (given as $\rho v^2 C_S$, where ρ is the mass density, v is the velocity, and C_S is the sound speed) at the bottom of the computational domain and at 400 km height. At the bottom border, the energy flux has a peak at 3.3 mHz and a high-frequency maximum at about 15 mHz, with a slow decline up to 50 mHz. Above 50 mHz there is no significant power. The propagating waves are damped by radiation as a function of frequency (Carlsson & Stein 2002), which gives less energy flux for higher frequencies, as seen in the figure. The ratio of the total energy fluxes at the bottom and at 400 km for the three frequency bins 5–20, 21–35, and 36–50 mHz are 3.07, 8.74, and 22.64, respectively.

Figure 3 displays the mean irradiance resulting from our numerical simulations compared to irradiance observations from the Solar Ultraviolet Spectral Irradiance Monitor (SUSIM) *ATLAS-3* mission on 1994 November 13 (Brueckner et al. 1994). To obtain the same resolution for the simulated irradiance as for the observed irradiance, we convolved the simulated irradiance with a Gaussian kernel. From the figure we see that the simulated irradiance fits well with the observed one up to about 1700 Å, except for a minority of emission lines that we have not included. Between 1700 and 1900 Å the simulated irradiance is up to a factor of 2 times the observed irradiance. In this area Si and Fe are the dominating continuum opacity sources. Iron is treated in LTE in the simulations, and we may also be missing line opacity in this region. The observed irradiance with emission lines excluded integrated over the *TRACE* passbands are 20% lower than in the simulations in the 1600 Å passband and 26% lower in the 1700 Å passband. The possible cause of this discrepancy and the effects on the results are discussed in § 4. We have also compared the simulated intensities with real *TRACE* images in the 1600 and 1700 Å passbands using the preflight calibration and find an agreement to better than 20%.

3. RESULTS

The outcome of our numerical simulations is the intensity as a function of frequency and time. To investigate the possibility of detecting high-frequency acoustic waves with *TRACE*, we need to transform this intensity into the two signals seen through the *TRACE* 1600 and 1700 Å passbands. To do this we multiply the intensity with the *TRACE* filter transmission functions (found using SolarSoft).[1] The result is shown in Figure 4. The *TRACE* signal is then obtained by integrating this function over wavelength. The *TRACE* filter transmission functions are broad, 275 and 200 Å, and are almost identical at the long end of the spectrum. The 1600 Å passband, however, stretches farther down toward the short-wavelength end than does the 1700 Å passband.

[1] See http://www.lmsal.com/solarsoft.

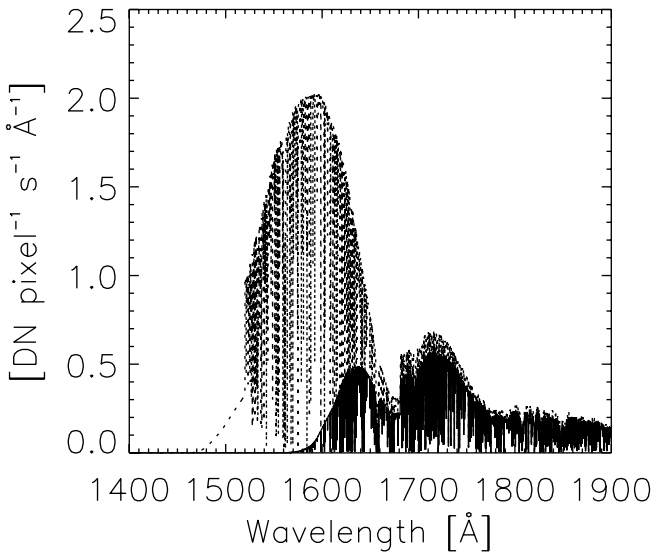

FIG. 4.—Intensities from the simulations multiplied with the *TRACE* 1600 Å (*dotted lines*) and 1700 Å (*solid lines*) filter transmission functions.

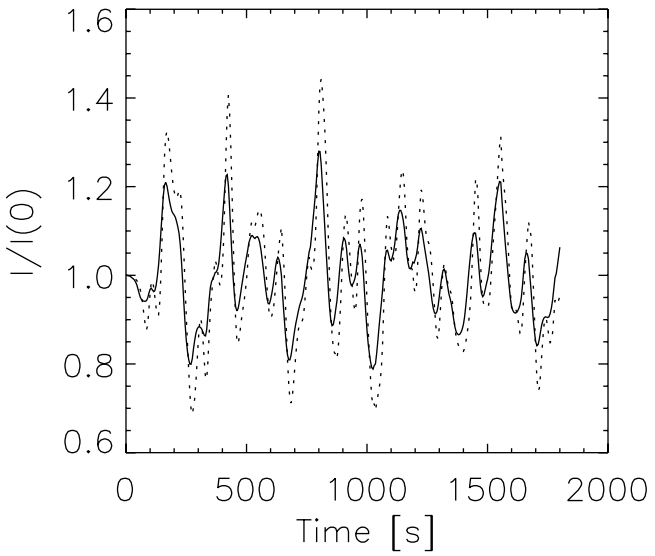

FIG. 5.—Normalized intensities from the simulations folded with the *TRACE* 1600 Å (*dotted line*) and 1700 Å (*solid line*) filter transmission functions.

The two intensities as functions of time obtained from the simulations are seen in Figure 5. From the figure it can be seen that the 1700 intensity (hereafter I_{1700}) is leading the 1600 intensity (hereafter I_{1600}), which implies that there are phase differences in the data. The phase differences are discussed in § 3.2. The amplitude of the I_{1600} signal is larger than the amplitude of I_{1700}. This is because I_{1600} is produced higher up in the atmosphere (see § 3.1), where the wave amplitude is larger. The amplitude is further enhanced by the increased sensitivity to temperature of the Planck function at shorter wavelengths.

Figure 6 displays the log power spectra of $\Delta I/I$; I_{1600} has here a greater amplitude compared to I_{1700} and retains power much longer and keeps some power down to 50 mHz, but after 40 mHz it is hard to distinguish this from noise. Correspondingly, there seems to be some power left of the I_{1700} at 50 mHz, but after 30 mHz the slope flattens out to be extremely slight. We know that the high-frequency piston in the bottom of the computational domain in the numerical simulations has no power above 50 mHz, so the intensity power plot should consist of purely white noise above 50 mHz.

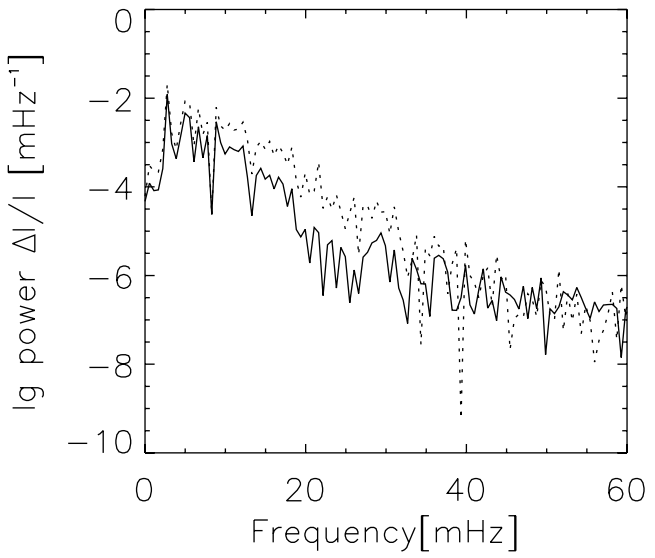

FIG. 6.—Log power spectra of $\Delta I/I$ as a function of frequency. *Solid line*: I_{1700}. *Dotted line*: I_{1600}.

3.1. *Response Functions*

There are various ways to determine formation heights of intensities. Uitenbroek (2004) calculated the optical depth unity of the continua at 1600 and 1700 Å in a cross section through a three-dimensional snapshot of a simulation of solar convection. He found the heights to vary between 300 and 550 km for 1600 Å and 150 and 350 km for 1700 Å with a mean at about 450 and 275 km, respectively.

We choose a different approach to finding the formation heights, namely, to calculate response functions. In general, a response function measures the response of an observed quantity to a given perturbation (Magain 1986). In this case the response function, $R_{I,T}(h)$, measures the response of $\Delta I/I$ given a perturbation in the temperature. The function is defined from

$$\frac{\Delta I}{I} = \int_{-\infty}^{\infty} R_{I,T}(h)\,\frac{\Delta T(h)}{T}\,dh, \tag{1}$$

where $R_{I,T}(h)$ is derived numerically from the simulations by using a step function to introduce a change of 1% in the temperature up to a given point in the atmosphere and varying this point. The intensities were calculated with silicon in non-LTE, once for each of the steps, and the resulting intensities were derived with regard to the depth giving the response function.

It is important to bear in mind that the response functions depend on the background atmosphere. In this article we are simulating a quiet area of the Sun, and the background atmosphere has no temperature rise in the lower chromosphere (see Fig. 1). We only include the effect of a changed temperature without taking into account the accompanying changes to the mass density and electron density one would get for a real perturbation.

The response functions are displayed in Figure 7. The two vertical lines in the figure show the heights where we found the best correlation of the intensities with the local temperature using scatter plots. These formation heights are approximately 360 and 430 km for I_{1700} and I_{1600}, respectively. However, this is only a mean, since the response functions are so broad.

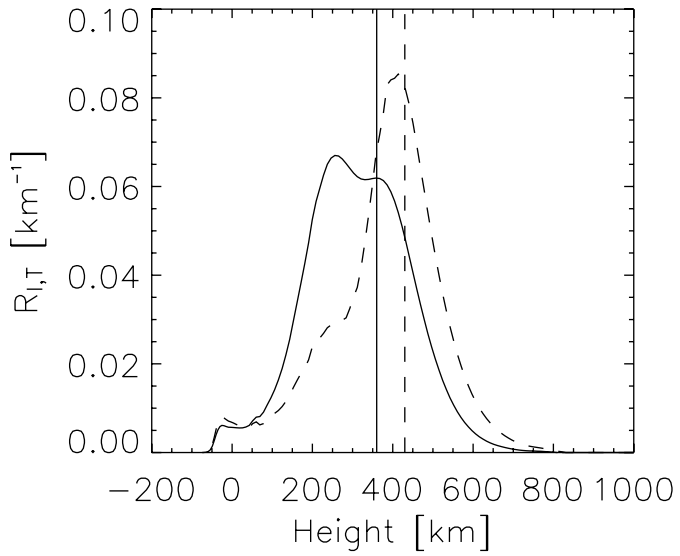

FIG. 7.—Response function of $\Delta I/I$ given a perturbation in the temperature, $\Delta T/T$. The vertical lines give the height of the maximum correlation between the intensity and the local temperature. *Solid lines*: I_{1700}. *Dotted lines*: I_{1600}.

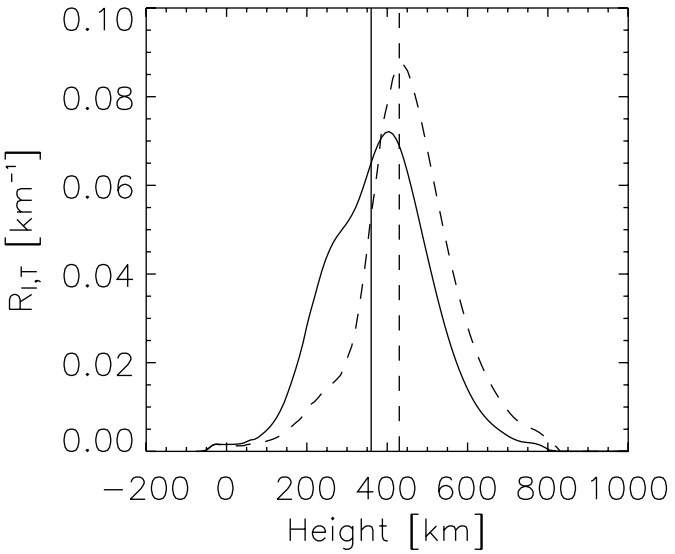

FIG. 8.—Response function of $\Delta I/I$ weighted by $(\rho/\rho_{400\,\mathrm{km}})^{-1/2}$ given a perturbation in the temperature, $\Delta T/T$. The vertical lines give the height of the maximum correlation between the intensity and the local temperature. *Solid lines*: I_{1700}. *Dotted lines*: I_{1600}.

FWHM of the response functions are 325 and 185 km for the 1700 and 1600 filters. Note also that the height of best correlation of the intensities with the local temperature of the simulation is higher than the average height of the response function. This is because the perturbation in temperature increases with height for an acoustic wave propagating in an atmosphere with exponentially decreasing density. Figure 8 displays the response function multiplied with an approximation for $\Delta T(h)/T$, assuming this perturbation to be proportional to $(\rho)^{(-0.5)}$. Now the height of best correlation fits perfectly well with the response functions.

We saw from the power plots that I_{1600} retains power to higher frequencies than I_{1700}. The explanation for this lies in the widths of the response functions; $R_{I1600,T}$ is much more narrow than $R_{I1700,T}$, so more high frequent waves will therefore pass through the former and still have significant power. For comparison, with a sound speed of 7 km s^{-1} a width of 185 km corresponds to the wavelength of a wave with frequency of 37 mHz, while 325 km corresponds to the wavelength of a wave of only 21 mHz.

3.2. *Phase Difference and Coherence*

Our definition of phase difference and coherence are the same as described in Krijger et al. (2001). The first plot in Figure 9 displays the degree of coherence between the two intensities. The signals are coherent up to about 20 mHz from where at least one of the signals is dominated by noise. For higher frequencies the coherence drops toward zero. From the bottom graph we can see the phase difference of I_{1600} and I_{1700}. It follows the expected behavior of propagating acoustic waves (the gray line shows the expected phase difference for acoustic waves propagating at 7 km s^{-1} and a height difference of 70 km) up to about 12 mHz. There it declines toward zero again and scatters. The scatter in phase corresponds to where the coherence between the signals is lost, but the turndown of the phase occurs when the coherence is still rather high. In the observations of Krijger they saw the same behavior of their phase differences. They attribute the turning down of the phase difference to acoustic waves steepening into weak shocks on their way up. The waves in our simulations do not steepen sufficiently at the response heights of the *TRACE* filters to support this explanation.

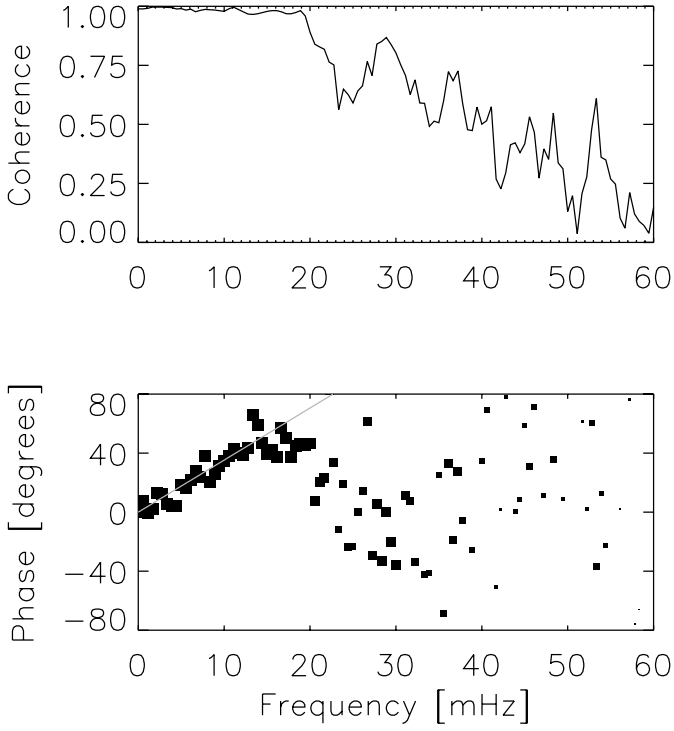

FIG. 9.—Coherence and phase difference of I_{1600} and I_{1700} as a function of frequency. The gray line is the phase difference of acoustic waves assuming a constant velocity of 7 km s^{-1} and a height difference of 70 km. The size of the symbols in the bottom panel is weighted according to the coherence in the top panel.

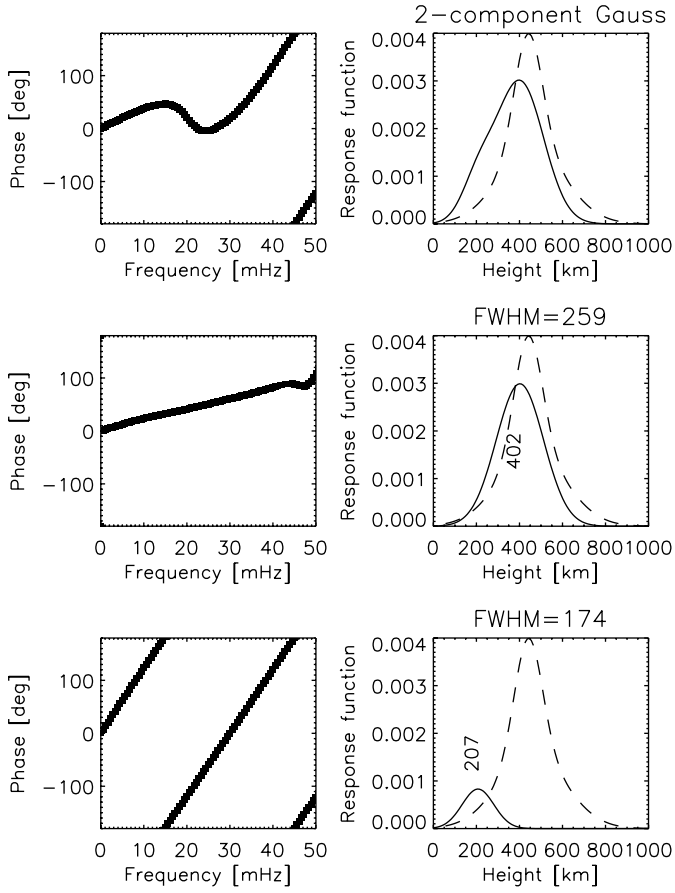

FIG. 10.—Phase difference (*left panels*) of sinusoidal waves convolved with various response functions (*right panels*): two-component fits to the response functions of Fig. 8 (*top*), wide component only for $R_{I1700,T}$ (*middle*), and narrow component only for $R_{I1700,T}$ (*bottom*).

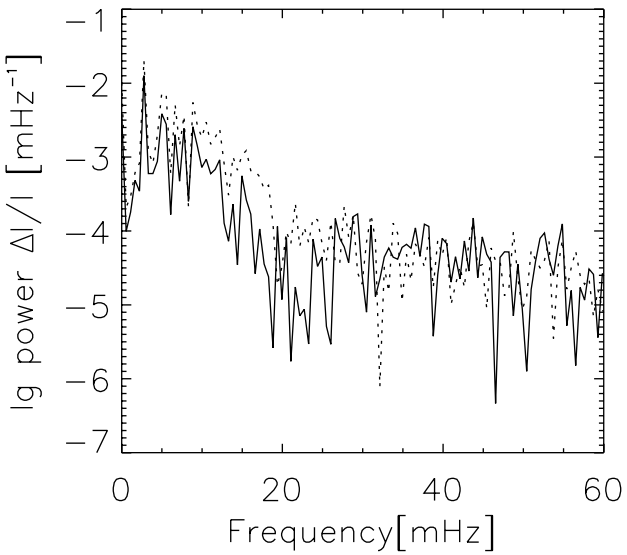

FIG. 11.—Log power spectra of $\Delta I/I$ including Poisson noise as a function of frequency. *Solid line*: I_{1700}. *Dotted line*: I_{1600}.

3.3. *Simple Sine Wave Simulations*

To try to establish the reason for the strange shape of the phase difference plot, we make simple numerical experiments by convolving signals of sine waves with the two response functions. Our simple waves consist of a sum of sine waves with different frequencies, all with the same amplitude and propagating at 7 km s^{-1}. The initial phases are set random.

When using the density-weighted response functions (Fig. 8) we obtain the same shape in phase difference as we did in the previous section. Exchanging the response functions with single-component Gaussian fits give a very different behavior; the phase follows the prediction for a propagating acoustic wave until the coherence drops and the phases scatter: there is no turndown of the curve. Replacing the response functions with two-component Gaussian fits produces the original behavior. It is especially $R_{I1700,T}$ that shows a double-peaked nature with the two components centered at 402 and 208 km with widths (FWHM) of 259 and 174 km, respectively. Figure 10 shows the phase diagram that results from the two-component Gaussian fits and from the individual components of the $R_{I1700,T}$. For low-frequency waves it is the wide component that dominates. For higher frequencies, the signal from the wide component is more attenuated than from the narrow component. The gradual shift from the wide component to the narrow component gives the turndown of the phase difference curve. For even higher frequencies the combined curve is very similar to the phase difference curve from the narrow component alone. The response function has a form equivalent to the sum of not only two components but also a large number of narrow components. The total phase difference for the highest frequencies with significant coherence will then be the sum of all the individual components resulting in a phase difference close to zero.

3.4. *Effect of Poisson Noise*

Finally, we want to find how the observational noise from *TRACE* interferes with analysis of the intensity signal. To observe 40 mHz waves we need a cadence of less than 12.5 s. A typical low compression high-cadence observing program with the 1600 and 1700 filters of *TRACE* has exposure times of 1.7 s for 1600 and 4.9 s for 1700. We now "observe" the simulated intensities through the *TRACE* telescope adding Poisson noise to our observations according to these exposure times. We have 30 minutes of simulations equivalent to 30 minutes of observations in only 1 pixel. The resulting intensities have a considerable amount of high frequent noise added; see Figure 11. However, even though the noise level has increased with a factor of almost 1000, we are still able to see power up to 20 mHz for I_{1700} and 25 mHz for I_{1600}.

4. DISCUSSION AND SUMMARY

We conclude from the simulations outlined in this paper that it would be possible to detect high-frequency acoustic waves up to at least 40 mHz using *TRACE*, in the absence of any instrumental noise. The noise limits the signal to 25 mHz and needs to be reduced with a factor of at least 100 to see waves at 40 mHz. If our aim is to study phase difference properties between the filter intensities, we are limited to waves below 30 mHz. Noise limits the signal to 20 mHz.

Waves above 40 mHz are difficult to see because of the very broad response functions caused by the wide band filters of *TRACE*. The filters span from including almost continuum regions to regions dominated by strong spectral lines. Having FWHMs of 325 and 185 km, the response functions gave us the mean formation heights of the I_{1700} and I_{1600} at 360 and 430 km.

The detectability limits given here take as a starting point a given amount of acoustic power fed into the simulation. We have here used a velocity piston based on the highest acoustic power given by theoretical studies of acoustic power generation by turbulence in the solar convection zone. If the real power present in the Sun is lower, then of course the intensity signal in the *TRACE* filters will be correspondingly lower.

The calculated solar irradiance is higher above 1700 Å than observations with SUSIM (Fig. 3), although calculated count rates are consistent with *TRACE* observations to within 20%. The higher intensities in the simulations could come from the neglect of line cooling in the upper photosphere in the hydrodynamic models and thus an overestimate of the temperature. The effect on including this missing cooling would be increased radiative damping of the waves in this region and a decreased signal. Including the missing opacity would also shift the response heights upward in the atmosphere. This would increase the signal (because of the increase in amplitude with height of acoustic waves) and increase the detectability of high-frequency waves. Given the fact that the integrated intensity convolved with the *TRACE* filter functions is close to the observed one, the possible error is judged to be small. The neglect of non-LTE effects in the iron continua (which are important for the intensity above 1682 Å) will have a small effect on the 1700 signal and almost none on the 1600 signal.

This work was supported by the Research Council of Norway grant 146467/420 and a grant of computing time from the Program for Supercomputing.

REFERENCES

Athay, R. G., & White, O. R. 1978, ApJ, 226, 1135
———. 1979a, ApJS, 39, 333
———. 1979b, ApJ, 229, 1147
Biermann, L. 1948, Z. Astrophys., 25, 161
Brueckner, C., Floyd, L. E., Lund, P. A., Prinz, D. K., & Vanhoosier, M. E. 1994, in IAU Colloq. 143, The Sun as a Variable Star: Solar and Stellar Irradiance Variations, ed. J. M. Pap, C. Frolich, H. S. Hudson, & S. Solanki (Cambridge: Cambridge Univ. Press), 72

Carlsson, M., & Stein, R. 1990, in Proc. of the Mini-Workshop on Physical Processes in the Solar Transition-Region and Corona, ed. P. Maltby & E. Leer (Oslo: Instit. Theor. Astrophys.), 177
———. 1992, ApJ, 397, L59
———. 1994, in Proc. Mini-Workshop on Chromospheric Dynamics, ed. M. Carlsson (Oslo: Instit. Theor. Astrophys.), 47
———. 1995, ApJ, 440, L29
———. 1997, ApJ, 481, 500
———. 2002, in Proc. IAU Colloq. 188, Magnetic Coupling of the Solar Atmosphere Euroconference, ed. H. Sawaya-Lacoste (ESA SP-505; Noordwijk: ESA), 293
Cunto, W., Mendoza, C., Ochsenbein, F., & Zeippen, C. J. 1993, Bull. Inf. Centre Donnees Stellaires, 42, 39
Deubner, F. L., Endler, F., & Staiger, J. 1984, Mem. Soc. Astron. Italiana, 55, 135
Deubner, F. L., & Fleck, B. 1990, A&A, 228, 506
Dorfi, E. A., & Drury, L. O. 1987, J. Comput. Phys., 69, 175
Fawzy, D., Rammacher, W., Ulmschneider, P., Musielak, Z. E., & Stepień, K. 2002, A&A, 386, 971
Goldreich, P., Murray, N., & Kumar, P. 1994, ApJ, 424, 466
Gustafsson, B. 1973, Uppsala Astron. Obs. Ann., 5, 6
Handy, B. N., et al. 1999, Sol. Phys., 187, 229
Krijger, J. M., et al. 2001, A&A, 379, 1052
Kurucz, R. L., & Bell, B. 1995, CD-ROM 23, Atomic Line Data (Cambridge: SAO)
Magain, P. 1986, A&A, 163, 135
Musielak, Z. E., Rosner, R., Stein, R. F., & Ulmschneider, P. 1994, ApJ, 423, 474
Rybicki, G. B., & Hummer, D. G. 1991, A&A, 245, 171
Scharmer, G. B., & Carlsson, M. 1985, J. Comput. Phys., 59, 56
Schwarzschild, M. 1948, ApJ, 107, 1
Stein, R. F., & Nordlund, Å. 2001, ApJ, 546, 585
Tobiska, W. K. 1991, J. Atmos. Terr. Phys., 53, 1005
Uitenbroek, H. 2004, in Proc. *SOHO* 13—Waves, Oscillations, and Small-Scale Transient Events in the Solar Atmosphere: A Joint View from *SOHO* and *TRACE*, ed. H. Lacoste (ESA SP-547; Noordwijk: ESA), 107
van Leer, B. 1974, J. Comput. Phys., 14, 361
Van Regemorter, H. 1962, ApJ, 136, 906
White, O. R., & Athay, R. G. 1979a, ApJS, 39, 317
———. 1979b, ApJS, 39, 347
Wunnenberg, M., Kneer, F., & Hirzberger, J. 2002, A&A, 395, L51